Topological transitions with an imaginary Aubry-André-Harper potential

Bofeng Zhu [1,2] Li-Jun Lang [3] Qiang Wang [1] Qi Jie Wang,[1,2,4,*] and Y. D. Chong [1,4,†]

[1]*Division of Physics and Applied Physics, School of Physical and Mathematical Sciences, Nanyang Technological University, Singapore 637371, Singapore*

[2]*School of Electrical and Electronic Engineering, Nanyang Technological University, Singapore 637371, Singapore*

[3]*Guangdong Provincial Key Laboratory of Quantum Engineering and Quantum Materials, School of Physics and Telecommunication Engineering, South China Normal University, Guangzhou 510006, China*

[4]*Centre for Disruptive Photonic Technologies, Nanyang Technological University, Singapore 637371, Singapore*

(Received 16 November 2022; accepted 27 March 2023; published 20 April 2023)

We study one-dimensional lattices with imaginary-valued Aubry-André-Harper (AAH) potentials. Such lattices can host edge states with purely imaginary eigenenergies, which differ from the edge states of the Hermitian AAH model and are stabilized by a non-Hermitian particle-hole symmetry. The edge states arise when the period of the imaginary potential is a multiple of four lattice constants. They are topological in origin, and can manifest on domain walls between lattices with different modulation periods and phases, as predicted by a bulk polarization invariant. Interestingly, the edge states persist and remain localized even if the gap in the real spectrum closes. These features can be used in laser arrays to select topological lasing modes under spatially extended pumping.

DOI: 10.1103/PhysRevResearch.5.023044

I. INTRODUCTION

The Aubry-André-Harper (AAH) model is a foundational theoretical model that illustrates the deep connections between quasicrystals, localization, and band topology [1–3]. It consists of a one-dimensional (1D) periodic discrete lattice, on which is applied a sinusoidal potential with a mismatched period. Varying the potential's period and phase produces an assortment of spectral gaps, which map to the band gaps of a two-dimensional (2D) quantum Hall lattice [3–6]. The boundary states in certain gaps of the 1D AAH model likewise map to topological edge states of the 2D lattice, which are linked to bulk topological invariants (Chern numbers). These interesting features have inspired numerous investigations into variants of the AAH model. For example, an AAH-type model with commensurate hopping modulations was found to have a separate class of topological boundary states [7]: zero modes whose energies are pinned to zero by particle-hole symmetry [8] and are linked to the topological properties of the Majorana chain [9].

Over the past decade, there has been increasing interest in *non-Hermitian* extensions of the AAH model [10–19], as part of a broader program to explore the properties and uses of non-Hermitian systems [20–22]. These models have included AAH-type lattices with parity/time-reversal (PT) symmetric gain/loss [10–13,17], and lattices with asymmetric hoppings violating both Hermiticity and reciprocity [14,18,19]. For example, PT-symmetric AAH models have been found to exhibit fractal spectra, similar to the Hermitian AAH model, in the real part of their eigenenergies [11]. Their PT symmetry breaking transition points also have interesting properties [12,13,17], such as governing the formation of boundary states [12] and mobility edges [17].

The boundary states in these non-Hermitian AAH models are directly related to the boundary states of the original AAH model. Similar persistence of topological boundary states into the non-Hermitian regime has been observed in other models; for example, in PT-symmetric Su-Schrieffer-Heeger (SSH) models [23–27], topological zero modes can be stabilized by particle-hole symmetry (as in the original Hermitian SSH model) or a non-Hermitian particle-hole symmetry [28,29]. Very recently, researchers have also found lattice models that host intrinsically non-Hermitian boundary states with no direct link to the Hermitian case [30–32]. For instance, Takata and Notomi discovered a periodic 1D lattice, with four atoms per unit cell, that hosts zero modes induced purely by gain and loss [32]. In view of these advances, it is worthwhile to examine zero modes in non-Hermitian AAH models. Can such modes be induced by gain/loss? What topological properties govern them, and how are they influenced by the AAH-style potential?

Here, we investigate a non-Hermitian AAH model with imaginary commensurate potentials. We find that when the modulation has period $\lambda = p/q$, where p and q are coprime integers and p is a multiple of 4, there arise topological boundary states whose energies have zero real part, which we refer to as "zero modes." The case of $\lambda = 4$ corresponds to the Takata-Notomi lattice [32]. The zero modes are stabilized by a non-Hermitian particle-hole symmetry [28,29], and are linked to a non-Hermitian topological invariant based on the electric

*qjwang@ntu.edu.sg
†yidong@ntu.edu.sg

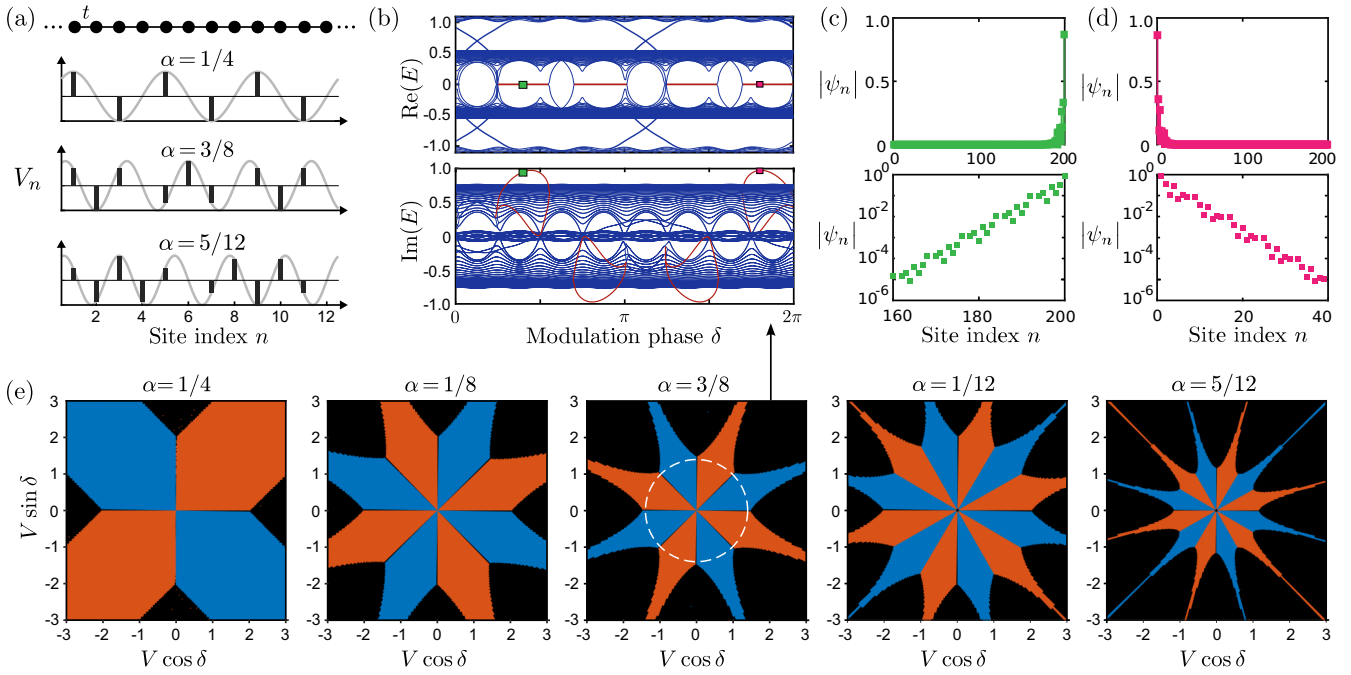

FIG. 1. (a) Schematic of a one-dimensional lattice with imaginary modulation. The model consists of a discrete chain with uniform nearest-neighbor hopping t (top panel), with imaginary on-site mass iV_n varying sinusoidally in space, with wave number $2\pi\alpha$. The bottom panels plot V_n versus site index n for $\alpha = 1/4$, $3/8$, and $5/12$ (black bars), along with the modulation profile (light gray curves). (b) Plot of the complex eigenenergies E versus modulation phase δ, for a finite lattice of size $N = 200$ with open boundary conditions. The model parameters are $V = 1.4$ and $\alpha = 3/8$, corresponding to the white dashes in (e). The zero modes are plotted in red. (c)–(d) Wave function magnitude $|\psi_n|$ versus site index n for the zero modes at (c) $\delta = 0.4\pi$ and (d) $\delta = 1.8\pi$, respectively indicated by the green and pink dots in (b). Lower panels are semilogarithmic plots for the sites nearest to one lattice boundary, showing that the zero modes are exponentially localized at the boundary. (e) Phase diagrams for different α, with orange (blue) regions indicating gaps at $\mathrm{Re}(E) = 0$ that are topologically nontrivial (trivial) according to the polarization and global Berry phase invariants calculated from the bulk band structure (see Appendix B). In the black regions, the real part of the bulk spectrum is gapless at $\mathrm{Re}(E) = 0$.

polarization [33–36], which depends on the modulation parameters. We derive the topological phase diagrams, and show that they predict the existence of zero modes at domain walls between different modulation functions (including those with different periods). Interestingly, the zero modes can survive and retain their localized character even if the gap in the real spectrum closes.

As the zero modes are governed by an imaginary sinusoidal potential, it may be possible to use them for mode selection in laser arrays. In existing implementations and proposals for topological lasers [26,27,37–46], including those based on the 1D SSH lattice [37,38,43] or its PT-symmetric variant [26,27], it is typically necessary to selectively pump the spatial regions where the desired topological modes are localized [26,27,37–45]. This induces the topological modes, rather than the numerous other nontopological modes, to lase. Using our non-Hermitian AAH model and its zero modes, a topological lasing mode can be selected via a spatially extended pump, such as the interference pattern formed by two optical pumping beams. The topological lasing mode can even be enabled or disabled by tuning the phase and period of the pumping pattern.

II. MODEL

We consider a one-dimensional chain with coupling t between nearest neighbors and a purely imaginary on-site potential described by a sinusoidal modulation, as depicted in Fig. 1(a). The Schrödinger equation is

$$t(\psi_{n+1} + \psi_{n-1}) + iV_n\psi_n = E\psi_n,$$
$$V_n = V\sin(2\pi\alpha n + \delta), \tag{1}$$

where ψ_n is the wave function at site n, E is the eigenenergy, and V, α, and δ are the amplitude, inverse period, and phase of the potential modulation function. We will set the unit of energy so that $t = 1$. We consider rational values of $\alpha = q/p$, where p and q are coprime positive integers; hence, the modulation function is commensurate with the underlying lattice, and the model is periodic with p sites per unit cell [3].

If p is even, the bulk Hamiltonian $\hat{\mathcal{H}}_k$ (a $p \times p$ matrix) satisfies the non-Hermitian particle-hole symmetry [29]

$$-\hat{\mathcal{H}}_k = \hat{\mathcal{C}}\hat{\mathcal{T}}\hat{\mathcal{H}}^*_{-k}\hat{\mathcal{T}}\hat{\mathcal{C}} = \hat{\mathcal{C}}\hat{\mathcal{T}}\hat{\mathcal{H}}^\dagger_k\hat{\mathcal{T}}\hat{\mathcal{C}}, \tag{2}$$

where $\hat{\mathcal{C}} = I_{p/2} \otimes \sigma_z$, with $I_{p/2}$ denoting the $p/2 \times p/2$ identity matrix and σ_z denoting the third Pauli matrix, and $\hat{\mathcal{T}}$ is the complex conjugation (time-reversal) operator. Equation (2) implies that the bulk eigenstates either occur in pairs with energies $\{E_1, E_2\}$ satisfying $\hat{E}_1(k) = -\hat{E}^*_2(k)$, or form a flat band with purely imaginary energy [29]. Moreover, for a finite lattice with N sites (with N even), the Hamiltonian $\hat{H}$ obeys the non-Hermitian particle-hole symmetry

$$\{\hat{H}, \hat{C}\hat{T}\} = 0, \tag{3}$$

where $\hat{C} = \mathbf{I}_{N/2} \otimes \sigma_z$.

We will focus on the case of $p = 4\mathbf{N}$, where $\mathbf{N} \in \mathbb{Z}^+$. In this case, the bulk band structure can host a real line gap, meaning a gap in the real part of the spectrum [21,47], around $\mathrm{Re}(E) = 0$. Such a gap does not appear for other choices of α (see Appendix A). As an example, Fig. 1(b) plots the complex spectrum for $\alpha = 3/8$, using a lattice of $N = 200$ sites with open boundary conditions (OBC). In the bulk spectrum, calculated using periodic boundary conditions (PBC) with the same lattice parameters, the real line gap closes at $m\pi/4$, where $m \in \mathbb{Z}$. In Fig. 1(b), it appears that the gap does not fully close at certain of these points (e.g., at $\delta = \pi/2$), but this is a finite-size effect; for larger N, the OBC spectrum has gap closings at the same points as the PBC spectrum (for details, see Appendix C).

Within half of the gaps, the lattice with OBC exhibits eigenenergies with $\mathrm{Re}(E) = 0$, plotted as red curves in Fig. 1(b). The wave functions of these "zero modes" are exponentially localized to the lattice boundary, as shown in Figs. 1(c) and 1(d). The zero modes preserve the non-Hermitian particle-hole symmetry: each eigenvector $|\psi\rangle$ obeys $|\psi\rangle = e^{i\theta}\hat{C}\hat{T}|\psi\rangle$, where θ is some global phase factor [28]. Note also that the zero modes need not have $\mathrm{Im}(E) = 0$; in fact, we see from the lower panel of Fig. 1(b) that they can have larger $\mathrm{Im}(E)$ than the bulk states. We will explore the possibility of using this feature for lasing in Sec. IV. In Appendix E, we show that the "zero modes" are robust to the disorders preserving particle-hole symmetry.

In Fig. 1(b), we can also see some in-gap states in the other band gaps, away from $\mathrm{Re}(E) = 0$. These are similar to the topological boundary states of the original AAH model [3–6], and are not the focus of the present work.

Takata and Notomi [32] have studied the case of $p = 4$, $q = 1$, which corresponds to the repeating gain/loss sequence $\{g_1, -g_2, -g_1, g_2\}$. In particular, they noted the existence of zero modes induced by the imaginary potential. The present work extends these results to a wider range of gain/loss modulations based on non-Hermitian AAH models.

III. TOPOLOGICAL PHASES

The zero modes introduced in the previous section are linked to topological features of the non-Hermitian band structure. These are expressible using the non-Hermitian Berry connection, calculated via a biorthogonal product instead of the Hermitian inner product [48–50].

The non-Hermitian band topology can be characterized in two complementary ways (see Appendix B). The first approach involves the non-Hermitian generalization [33–36] of the electric polarization [51,52]. When there is a real line gap, we can calculate the non-Abelian, non-Hermitian Berry connection for all bands with $\mathrm{Re}(E) < 0$, and use the nested Wilson loop method [53–55] to integrate it around the Brillouin zone. This procedure has previously been shown to yield quantized polarizations in other non-Hermitian systems with real line gaps, e.g., non-Hermitian higher-order topological insulators [33]. The second approach to characterizing the band topology is the global Berry phase [26,32,49], which involves integrating the non-Hermitian Berry connections for all bands (with care taken to fix the gauge and sort the bands [56,57]; see Appendix B). Both methods are based on the bulk band structure, derived under PBC.

When there is a real line gap at $\mathrm{Re}(E) = 0$, the polarization and global Berry phase calculations are in agreement, and yield the topological phase diagrams shown in Fig. 1(e). These phase diagrams are plotted using the modulation parameters (V, δ) as polar coordinates, for various $\alpha = q/p$ with p, q coprime and p a multiple of 4. In the orange regions, the band structure gives quantized polarization $p_x = 1/2$ and a global Berry phase of 2π. In the blue regions, the polarization and global Berry phase vanish. In the black regions, there is no real line gap at $\mathrm{Re}(E) = 0$ and the polarization calculation is inapplicable; we will discuss the lattice's behavior in this regime later in this section. Evidently, the real line gap phases form p spokes in the phase diagram, extending outward from the origin $V = 0$, and alternating between trivial and nontrivial phases. The phase diagrams for other $\alpha = q/p$ are consistent with the pattern shown in Fig. 1(e).

To test whether the phase diagrams correctly predict the existence of zero modes, we examine the behavior at domain walls between different modulation functions [24,32,38,58–60]. The lattice shown in Fig. 2(a) consists of two adjacent domains with different gain/loss distributions. The two modulation functions have different α (3/8 and 1/4), as well as different δ, as indicated by the phase diagrams in the lower panels of Fig. 2(a). With the two domains chosen to be topologically inequivalent, we see that the complex spectrum, plotted Fig. 2(b), contains a zero mode (highlighted in green). Its wave function is exponentially localized to the domain wall, as shown in Fig. 2(c). [Note that this zero mode has the largest $\mathrm{Im}(E)$ among all the eigenstates; we will discuss the significance of this in Sec. IV. The other zero mode that can be seen in Fig. 2(b) is localized to the opposite end of the topologically nontrivial domain, rather than the domain wall.] In Appendix D, we show other combinations of modulation parameters, which all behave as expected. In particular, if the domains are both trivial or both nontrivial, there is no zero mode at the domain wall. This verifies that the zero modes arise from a non-Hermitian topological bulk-edge correspondence.

An interesting feature of the non-Hermitian zero modes is that they can persist for a short but nonzero interval after the closing of the real line gap in bulk spectrum, pinned to $\mathrm{Re}(E) = 0$. This contrasts with the Hermitian case, where the closing of the band gap causes zero modes and other localized boundary states to hybridize with bulk states and lose their localized character. In Fig. 3(a), we plot parametric trajectories in the $\alpha = 3/8$ phase diagram, extending into the gapless (i.e., no real line gap in bulk spectrum) phases to each side of the gapped phase. The complex band energies along these trajectories are plotted in Figs. 3(b) and 3(c). When the real line gap in the bulk spectrum closes, the complex-valued zero-mode energies and bulk energy bands (specifically, their imaginary parts) do not overlap. Hence, the zero modes remain spatially localized, as shown in Figs. 3(d) and 3(e). In Appendix C, we show that zero modes vanish by coalescing with each other at exceptional points [20,22], rather than hybridizing with bulk states; moreover, within the gapless phase, they are robust against disorder that preserves particle-hole symmetry (see Appendix E). Related behavior has recently been pointed out in the context of topological

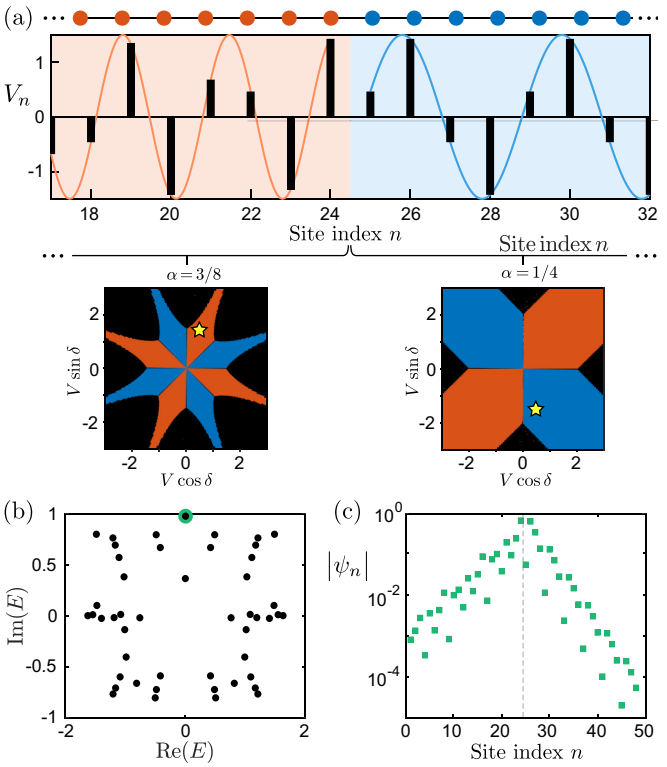

FIG. 2. (a) Lattice formed by joining two chains with different gain/loss modulations. In the upper panel, the left (right) domain, marked in orange (blue), is topologically nontrivial (trivial). In the middle panel, the black bars indicate V_n, the gain/loss on site n, and the solid curves plot the modulation functions, which notably have different periods in the two domains. For the left domain, $\alpha = 3/8$, $V = 1.5$, and $\delta = 0.4\pi$; for the right domain, $\alpha = 1/4$, $V = 1.5$, and $\delta = -0.4\pi$. In the lower panels, the phase diagrams for the two domains are shown, with the choice of modulation parameters marked by yellow stars. (b) Complex eigenenergy spectrum for the lattice, with a total of $N = 48$ sites (24 in each domain). The mirror symmetry around $\mathrm{Re}(E) = 0$ is due to the non-Hermitian particle-hole symmetry in Eq. (2). (c) Spatial distribution of the zero mode highlighted in green in (b). Vertical dashes indicate the domain wall.

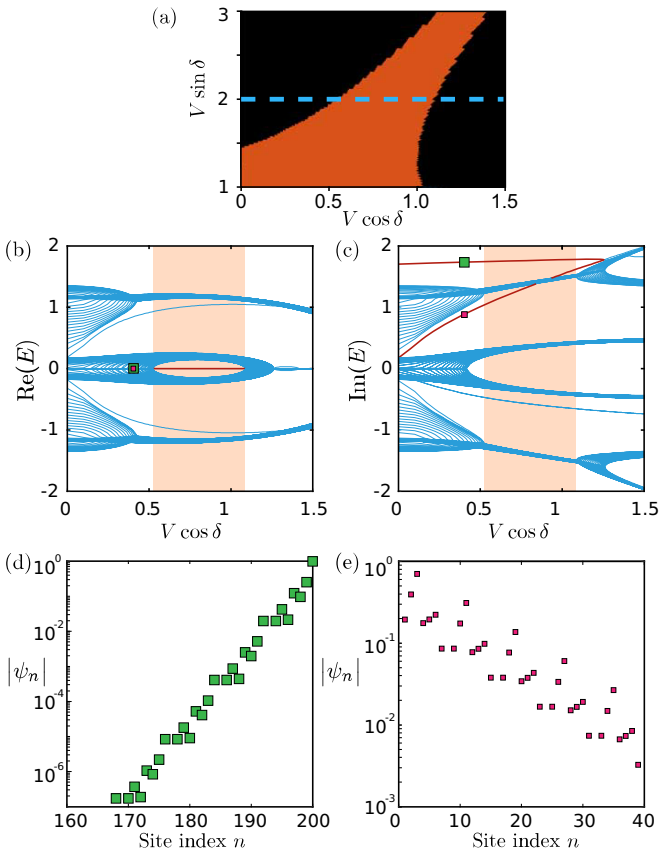

FIG. 3. (a) Close-up view of the phase diagram for $\alpha = 3/8$. Dashes indicate a trajectory corresponding to $V \sin\delta = 2$. (b)–(c) Complex eigenenergy spectrum corresponding to the dashes in (a), for lattice size $N = 200$. The ranges corresponding to the nontrivial real line gap phase of bulk spectrum are highlighted in orange. The topological zero modes, plotted in red, persist even when the real line gap in bulk spectrum closes, and remain exponentially localized to the boundary. (d)–(e) Spatial distribution of the zero modes at $V \cos\delta = 0.4$, marked by squares in (b)–(c).

crystalline insulators, where higher-order topological modes can persist despite having $\mathrm{Re}(E)$ degenerate with the bulk bands [61,62].

IV. MODE SELECTION IN LASER ARRAYS

The non-Hermitian AAH model can be used as the basis for a topological laser distinct from the other topological lasers studied to date [26,27,37–45,56]. It has previously been noted that lasers are a natural setting for realizing and exploiting non-Hermitian topological phenomena, since they necessarily contain gain (stimulated emission) and loss (outcoupling and material dissipation). Thus, for instance, researchers have implemented laser arrays based on the PT-symmetric SSH model, with lasing modes based on the non-Hermitian zero modes of that model [26,27].

In this context, the non-Hermitian AAH model's most striking feature is that its properties are governed directly by the gain/loss modulation function, whose period differs from (and can be significantly larger than) that of the photonic lattice. One interesting possibility is to excite the lattice using a sinusoidally varying pump profile, such as an interference pattern of two optical pumping beams. The period and phase of the pump profile could be easily varied to access different parts of the non-Hermitian AAH model's phase diagram.

To investigate this, we consider a laser model consisting of a non-Hermitian AAH chain with a *nonlinear* imaginary potential iV_n, where

$$V_n = \frac{\Gamma \lambda_n}{1 + |\psi_n|^2} - \gamma. \tag{4}$$

Here, Γ is an overall pump strength, $\lambda_n \in [0, 1]$ is the normalized sinusoidal modulation, $|\psi_n|^2$ is the local intensity on site n, and γ is a passive loss rate (which can include outcoupling loss). The $1 + |\psi_n|^2$ denominator represents the effects of gain saturation [28,39]. Taking $\alpha = 3/8$, $\delta = 0.4\pi$, and $\gamma = 3$, we performed time-domain simulations by numerically integrating the nonlinear equation $i\partial_t|\psi\rangle = H(|\psi\rangle)|\psi\rangle$ [28,39,63]. The wave function is initialized to the random values $\psi_n(t = 0) = (\alpha_n + i\beta_n)f_0$, where α_n, β_n are drawn

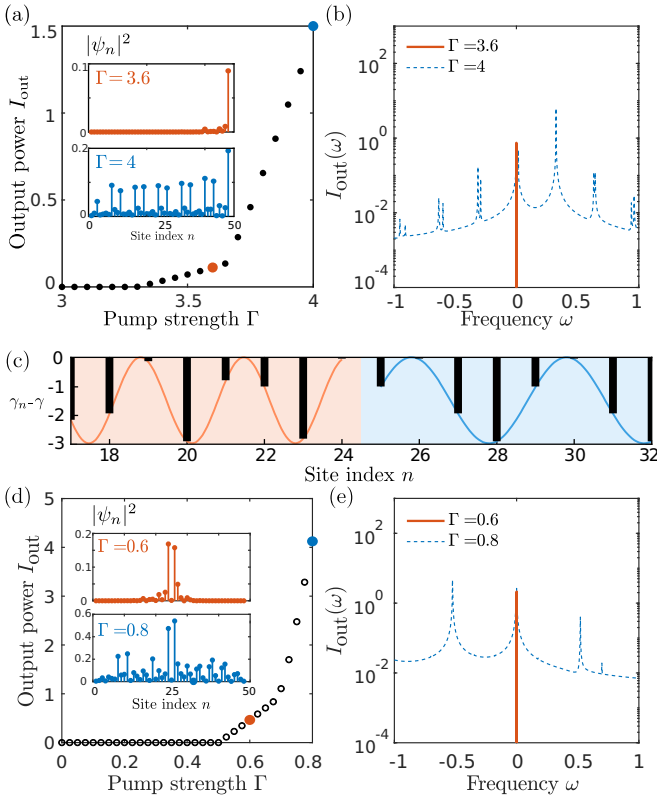

FIG. 4. (a)–(b) Simulation results for a laser with a spatially modulated pump strength, given by Eq. (4). The lattice consists of a single domain with $\alpha = 3/8$, $\delta = 0.4\pi$, and size $N = 48$, with passive loss rate $\gamma = 3$. (a) Output intensity I_{out} versus pump strength Γ. Inset: Spatial distribution of $|\psi_n|^2$ at $t = 5000$ for $\Gamma = 3.6$ (top) and $\Gamma = 4$ (bottom). (b) Output spectrum for $\Gamma = 3.6$ (orange line) and $\Gamma = 4$ (blue dashes). (c)–(e) Simulation results for a laser with spatially modulated loss and uniform pump strength, given by Eq. (5), with lattice size $N = 48$. (c) Spatial distribution of the loss term $\gamma_n - \gamma$ (black bars), along with the underlying modulation functions. These modulation functions form a domain wall in the center of the lattice, and are identical to those of Fig. 2 up to a constant offset. (d) Output intensity I_{out} versus pump strength Γ. Inset: Spatial distribution of $|\psi_n|^2$ at $t = 5000$ for pump strengths $\Gamma = 0.6$ (top) and $\Gamma = 0.8$ (bottom). (d) Output spectrum at $\Gamma = 0.6$ (orange line) and $\Gamma = 0.8$ (blue dashes).

independently from the standard normal distribution, n is the site index, and $f_0 = 0.01$ is a scale factor. The simulated time interval is $t \in [0, 5000]$, long enough for transient oscillations to cease. The laser output I_{out} is obtained by averaging the on-site intensities $|\psi_n|^2$ over the evolution interval of $t \in [2000, 5000]$ (we assume equal outcoupling from each site, with normalized power units).

The resulting plot of I_{out} versus pump strength Γ is shown in Fig. 4(a). Because the zero mode of the linear lattice has (in this case) the highest relative gain, it lases first. As shown in the inset of Fig. 4(a), the frequency spectrum at $\Gamma = 3.6$ consists of a single peak at $\omega = 0$. (Note that in an actual laser, ω is a frequency detuning, relative to the natural frequency of the decoupled resonators.) The intensity is localized to one boundary of the lattice, as shown in the upper panel of the inset in Fig. 4(a). These two features of the lasing mode—the pinning of the frequency to $\omega = 0$ and the spatial localization—are inherited from the linear non-Hermitian AAH model, and are selected by the choice of the pump's spatial modulation λ_n, which can be easily adjusted (e.g., by changing the interference pattern of an optical pump). When Γ is further increased, the additional modes of the lattice also start to lase (see Appendix F), and the system enters the multimode lasing regime, as shown for the case of $\Gamma = 4$ in Fig. 4(b) and the bottom panel of the inset in Fig. 4(a).

An alternative way to access the non-Hermitian AAH model with a laser array is to use loss engineering. We can modulate the (linear) loss on individual sites, and then pump the entire lattice, as described by the imaginary potential iV_n, where

$$V_n = \frac{\Gamma}{1 + |\psi_n|^2} + \gamma_n - \gamma. \tag{5}$$

For this case, we suppose $\gamma_n - \gamma$ is formed by two modulation functions with a domain wall at the center, as shown in Fig. 4(c). Within each domain, $\gamma_n = V \sin(2\pi\alpha n + \delta)$, and we pick the same values of V, α, and δ as in Fig. 2. We also include an additional constant loss $\gamma = \mathrm{Im}(E_0) + 0.5$, where E_0 is the eigenenergy of the desired zero mode [square marker in Fig. 2(b)]. As shown in Fig. 4(d), this sets the laser threshold to $\Gamma = 0.5$. For some range of pump strengths above threshold, the lasing frequency is pinned to $\omega = 0$ and localized at the domain wall, as shown in Fig. 4(e) and the upper panel of Fig. 4(d) for pump strength $\Gamma = 0.6$. Multimode lasing is observed at higher pump strengths (e.g., $\Gamma = 0.8$). Although the spatial modulation in the lattice recalls the conventional distributed-feedback (DFB) laser, the basic mechanism is quite different, as the spatial modulation in DFB lasers only provides reflection (optical feedback), while the imaginary AAH-style potential alters the topology properties and gives rise to topologically protected edge modes. The laser design proposed here also differs from previous 1D topological lasers [26,27], which were based on the SSH model and its non-Hermitian variants. In particular, the topological modes of the SSH lasers are inherited from the Hermitian SSH model, whereas the present topological phases are generated from non-Hermitian gain/loss modulations.

V. DISCUSSION

We have demonstrated that a non-Hermitian variant of the AAH model, consisting of a sinusoidally modulated potential that is not real but rather purely imaginary, can exhibit topological boundary modes with purely imaginary energy. These zero modes are found when the modulation period is a multiple of four lattice constants, and are pinned to $\mathrm{Re}(E) = 0$ by an unbroken non-Hermitian particle-hole symmetry [28]. Our results generalize the period-four lattice found by Takata and Notomi [32] to a wider family of AAH-type imaginary potentials. The complex band structure has two distinct phases with real line gaps at $\mathrm{Re}(E) = 0$, characterized by non-Hermitian topological invariants. The invariants correctly predict the existence of zero modes, even for domain walls between modulations with different periods.

Previously, Hermitian zero modes have been observed in a variant of AAH model that has commensurate modulations in

the hoppings (rather than the on-site potential) [7]. However, that model was based on a Hermitian particle-hole symmetry different from Eq. (2), and we have not found any deeper relationship between these sets of results.

In the non-Hermitian AAH model, it is possible to tune the imaginary potential so that the zero modes can have the highest relative gain of all the eigenstates. This property can be exploited for mode selection in laser arrays, as we showed using simulations. One interesting possibility is to use optical pumping beams in an interference pattern (corresponding to spatially modulated gain) to control the lasing of the zero modes; alternatively, one can modulate the loss in the laser array and pump uniformly. In both cases, our simulations results show that a non-Hermitian zero mode can be the first lasing mode, and retain its key characteristics (frequency pinning and spatial localization) from the lasing threshold up to the onset of multimode lasing.

ACKNOWLEDGMENTS

This work was supported by the A*STAR Programmatic Funds No. A18A7b0058, the Singapore MOE Academic Research Fund Tier 3 Grant No. MOE2016-T3-1-006, Tier 2 Grant No. MOE2019-T2-2-085, Tier 1 Grant No. RG148/20, and the Singapore National Research Foundation (NRF) Competitive Research Program (CRP), Grants No. NRF-CRP18-2017-02 and No. NRF-CRP23-2019-0007; L.-J.L. was supported by the National Natural Science Foundation of China (Grant No. 11904109) and the Guangdong Basic and Applied Basic Research Foundation (Grant No. 2019A1515111101).

APPENDIX A: BULK BAND STRUCTURES FOR $\alpha = 1/6$ AND LINE GAP WIDTH

In this section, we discuss the band structure for $\alpha = q/p = 1/6$. This is representative of the behavior for other p values that are even but not a multiple of 4 (i.e., $p = 2, 6, 10, \ldots$). The bulk Hamiltonian is

$$\mathcal{H}_k = \begin{bmatrix} iV_1 & t & & te^{-ik_x} \\ & \ddots & & \\ te^{ik_x} & & t & iV_n \end{bmatrix}, \tag{A1}$$

where $n = 1, 2, \ldots, 6$ is the site index within the unit cell, and the V_n is the value of the modulation function $V \sin(2\pi\alpha n + \delta)$ on site n.

The complex eigenenergy spectrum $\{E_{mk}\}$ (where m is the band index) consists of the eigenvalues of $\mathcal{H}_k$ for $k \in [-\pi, \pi]$. Figure 5(a) plots $\mathrm{Re}(E_{mk})$ versus k and the modulation amplitude V, while Fig. 5(b) plots the band structures for $V = 0$.

In the absence of the imaginary modulation ($V = 0$), there are six cosinusoidal bands with degeneracies at $k = 0, \pi$, with one of the $k = \pi$ degeneracies occurring at $E = 0$, as shown in Fig. 5(b). For $V \neq 0$, the real band gap around $\mathrm{Re}(E) = 0$ remains closed, and instead an imaginary band gap appears around $\mathrm{Im}(E) = 0$, as shown in Fig. 5(c).

We have also investigated the width of the real line gap for different p and q. Figure 6 plots the gap widths against $V\cos\delta$ and $V\sin\delta$, for lattices with periodic boundary conditions (PBC) and $\alpha = \{1/4, 1/8, 3/8, 1/12\}$. Smaller values of p produce a wider band gap, which tends to make the zero mode more robust against disorder (see Appendix E).

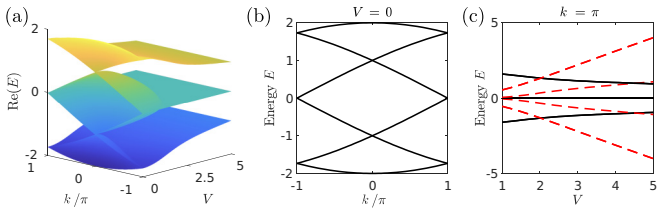

FIG. 5. (a) Evolution of the real bulk band structure with Bloch wave number k and modulation amplitude V, for $\alpha = 1/6$. (b) Bulk band structure for $V = 0$. (c) Complex bulk band energies at $k = \pi$ versus V, with the solid black and dashed red lines denoting the real and imaginary parts.

APPENDIX B: TOPOLOGICAL INVARIANTS

The calculation of the non-Hermitian polarization p_x follows previous analyses of non-Hermitian topological lattices [33,36,50]. First, we define a generalized complex-valued Berry connection,

$$[A_k]^{mn} = i\frac{\langle u^{\mathrm{L}}_{m,k}|\partial_k u^{\mathrm{R}}_{n,k}\rangle}{\langle u^{\mathrm{L}}_{m,k}|u^{\mathrm{R}}_{m,k}\rangle\langle u^{\mathrm{L}}_{n,k}|u^{\mathrm{R}}_{n,k}\rangle}, \tag{B1}$$

where m, n are band indices and L/R denote left/right eigenvectors. This definition is based on the fact that although the eigenvectors of a non-Hermitian Hamiltonian are not orthogonal, they obey a biorthogonality relation $\langle u^{\mathrm{L}}_m(k)|u^{\mathrm{R}}_n(k)\rangle = \delta_{mn}$. We also use a "nested" Wilson loop operator, defined using a base point k that progresses across the Brillouin zone until it

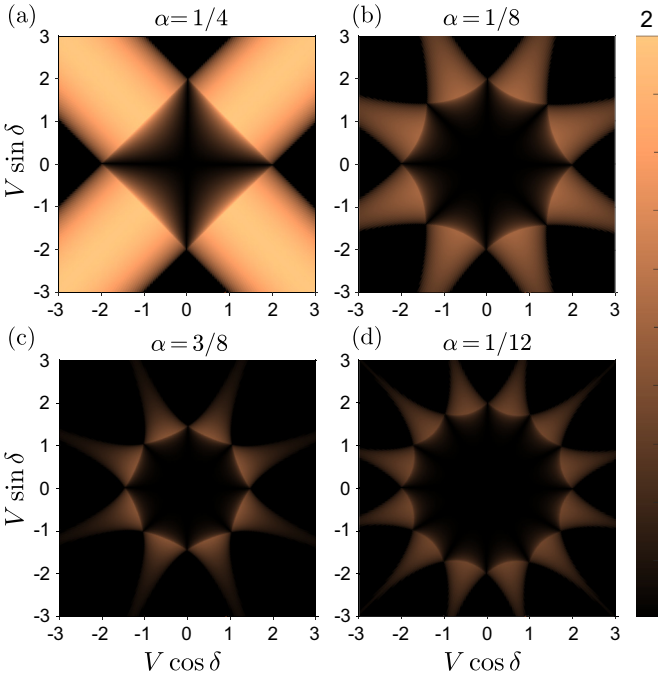

FIG. 6. Heat map of the width of the real line gap with model parameters, calculated using PBC with different modulation frequencies: (a) $\alpha = 1/4$, (b) $\alpha = 1/8$, (c) $\alpha = 3/8$, and (d) $\alpha = 1/12$.

reaches $k + 2\pi$ [33,36]:

$$W_{k+2\pi\leftarrow k} = G_{k+2\pi-\Delta k} \cdot G_{k+2\pi-2\Delta k} \ldots G_{k+\Delta k} \cdot G_k, \quad \text{(B2)}$$

where G_k is a rank $p/2$ matrix whose elements are

$$[G_k]^{mn} = \langle u_m^{\mathrm{L}}(k) | u_n^{\mathrm{R}}(k + \Delta k) \rangle. \quad \text{(B3)}$$

For a large lattice with a real line gap at $\mathrm{Re}(E) = 0$, the electric polarization is related to the Wilson loop by [36,55]

$$p_x = \frac{i}{2\pi} \ln \det \left[\int_k^{k+2\pi} A_k \, dk \right] = \frac{i}{2\pi} \ln \left(\det[W_{k+2\pi\leftarrow k}] \right), \quad \text{(B4)}$$

where the band indices of the A matrix only run over (say) the lower bands, i.e., those with $\mathrm{Re}(E) < 0$.

This procedure has previously been used to topologically characterize other non-Hermitian lattice models [36]. In the present work, we apply it to non-Hermitian AAH models with real line gaps at $\mathrm{Re}(E) = 0$. We find that either $|p_x| = 1/2$ (which we call the topologically nontrivial phase), or $p_x = 0$ (the topologically trivial phase). These results, obtained from the bulk (PBC) model, are found to match the presence or absence of topological edge modes in the finite (OBC) lattices.

Definition of global Berry phase. Suppose we have a non-Hermitian band indexed by n, whose right and left eigenvectors are denoted by $|\psi(n, k)\rangle$ and $|\lambda(n, k)\rangle$, where k is the Bloch wave number. The Berry phase over a k-space contour C can be defined as [49]

$$\phi_n = i \oint_C \langle \lambda(n, k) | \partial_k | \psi(n, k) \rangle \, dk. \quad \text{(B5)}$$

Liang and Huang [49] devised a "global Berry phase" that consists of the sum of the Berry phases for all bands,

$$\phi_G = \sum_n \phi_n. \quad \text{(B6)}$$

In exemplary non-Hermitian lattice models, such as a bipartite dissipative model [49] and a non-Hermitian Su-Schrieffer-Heeger (SSH) model [26], it has been found that discontinuities in ϕ_G, for a given gauge, coincide with topological phase transitions. However, it should be noted that gauge transformations cause ϕ_G to change by multiples of 2π, so the actual value of ϕ_G is not used to identify specific phases.

APPENDIX C: CLOSING OF THE REAL LINE GAP

In this section, we discuss the closing of the real line gap in the finite-size (OBC) lattice. In Fig. 1(b) of the main text, the bulk modes' real line gap appears not to fully close at certain points (e.g., near $\delta = \pi/2$); the spectrum is replotted in Fig. 7(a) for ease of reference. However, this can be shown to be a finite-size effect. Figure 7(b) presents a zoomed-in view of the spectrum near $\delta = \pi/2$. Figure 7(c) shows the spectrum for a much larger lattice size, $N = 2000$. In both Figs. 7(b) and 7(c), the gray-shaded regions indicate the range of eigenenergies for the infinite lattice, under PBC with phase shift swept through $k \in [0, 2\pi)$. Evidently, as N becomes large, the OBC spectrum approaches the PBC spectrum, and the bulk gap closes at $\delta = \pi/2$ as claimed. We find a similar situation for $\delta = 3\pi/4$, $\delta = 3\pi/2$, $\delta = 7\pi/4$, etc.

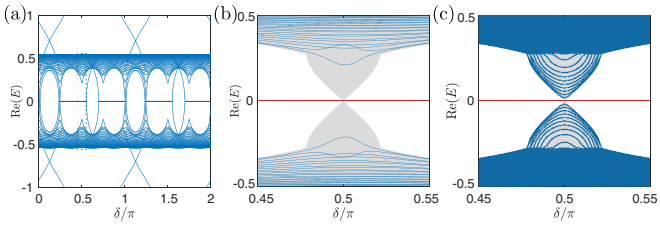

FIG. 7. (a) Real part of the bulk eigenenergies near $\delta = \pi/2$, for a finite lattice of size $N = 200$ with OBC. (b) Zoomed-in plot of the bulk band structure for a finite lattice of size $N = 2000$ with OBC. In (b)–(c), the gray-shaded regions indicate the eigenenergies under PBC, with $k \in [0, 2\pi)$. All other model parameters are the same as in Fig. 1(b) of the main text.

It can be seen in Figs. 7(b) and 7(c) that the zero modes persist to the right of the bulk gap closing at $\delta = \pi/2$. This is the persistence discussed in the last paragraph of Sec. III (and Fig. 3) in the main text. Unlike zero modes of Hermitian models, the zero modes of the non-Hermitian AAH model do not hybridize with the bulk states when the gap closes. Instead, two zero modes approach along the imaginary energy axis, and annihilate at an exceptional point (EP).

In Figs. 8(a) and 8(d), we plot $\mathrm{Im}(E)$ versus δ for the zero modes, close to the EP, for two different values of V. Figures 8(b) and 8(e) show the complex eigenenergy plots just before the EP, with the zero modes close to each other on the imaginary axis. Figures 8(c) and 8(f) show the spatial distributions of the zero modes; they are localized on the same boundary, consistent with the fact that they will eventually coalesce to the same eigenstate at the EP.

The boundary states that extend into the trivial phase can be shown to be "nonuniversal," in the sense that they are affected by disturbances to the boundaries. Figure 9(a) plots the real part of the complex eigenenergies for a finite lattice of length $N = 198$ (rather than $N = 200$ in the main text; this

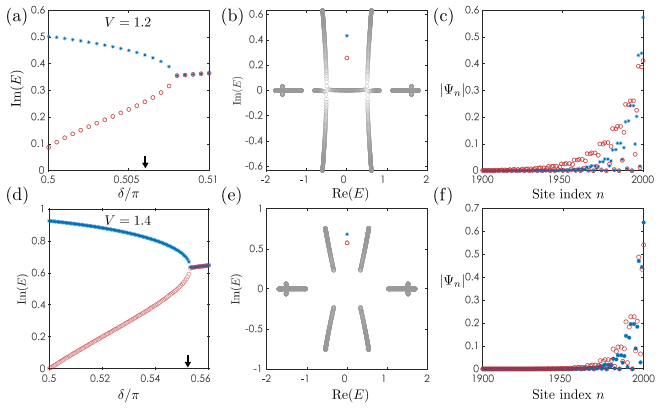

FIG. 8. (a) Plot of $\mathrm{Im}(E)$ versus δ for the boundary modes, in the vicinity of the bulk gap-closing point $\delta = 0.5\pi$. The modulation amplitude is $V = 1.2$. (b) Distribution of eigenenergies in the complex plane for a lattice of size $N = 2000$ with OBC, for the value of δ marked by an arrow in (a). The blue star and red hollow circle denote two zero modes whose energies lie along the imaginary axis. (c) Spatial distribution of the two eigenmodes marked in (b). (d)–(f) Similar to (a)–(c), but for $V = 1.4$.

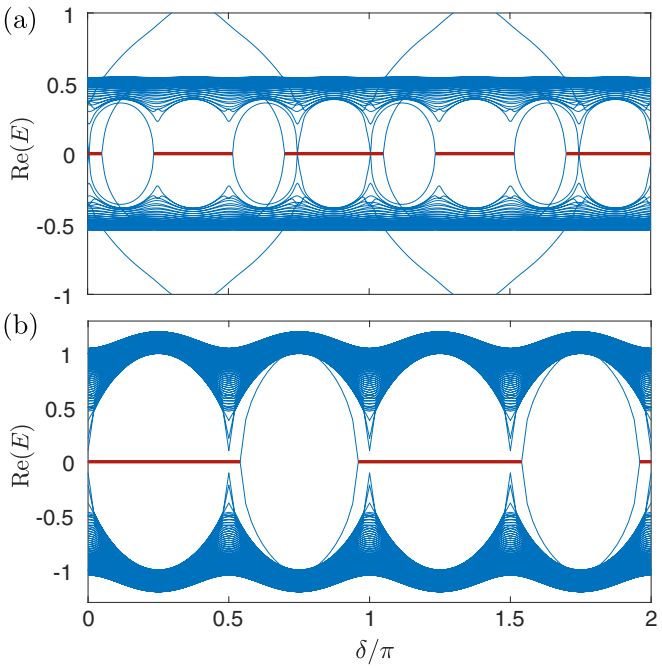

FIG. 9. Plot of the complex eigenenergies E versus modulation phase δ, for a finite lattice of size $N = 198$ with open boundary conditions. The model parameters are $V = 1.4$ and $\alpha = 3/8$ in (a) and $V = 1.9$ and $\alpha = 1/4$ in (b). The zero modes are plotted in red.

involves truncating a unit cell at the boundary). This shifts the range over which the zero modes exist in the trivial phase. However, they still exist throughout the nontrivial phase. The persistence of edge modes is not exclusive for $\alpha = 3/8$, and can be also observed with other modulation period, e.g., the case with $\alpha = 1/4$ in the paper by Takata and Natomi [32]. The complex eigenenergies of a finite lattice with $\alpha = 1/4$ and $V = 1.9$ are plotted in Fig. 9(b), while all the other parameters are the same as Fig. 9(a). In the figure, similar effects are also observed.

APPENDIX D: DIFFERENT DOMAIN WALL CONFIGURATIONS

In Fig. 10, we consider several domain wall configurations different from the one shown in Fig. 2 of the main text. Apart from the choices of modulation phase δ in each domain, all the other lattice parameters are the same as in Fig. 2 of the main text.

In the first case, both domains are topologically trivial, with parameters given by yellow stars in the phase diagrams of Fig. 10(a). We find that the complex spectrum of the OBC lattice lacks any eigenenergies at $\mathrm{Re}(E) = 0$, as shown in Fig. 10(b). In the second case, corresponding to the green stars in Fig. 10(a), both domains are topologically nontrivial. Here, we do observe zero modes, but they are not localized at the domain wall. For example, for the zero mode indicated by a

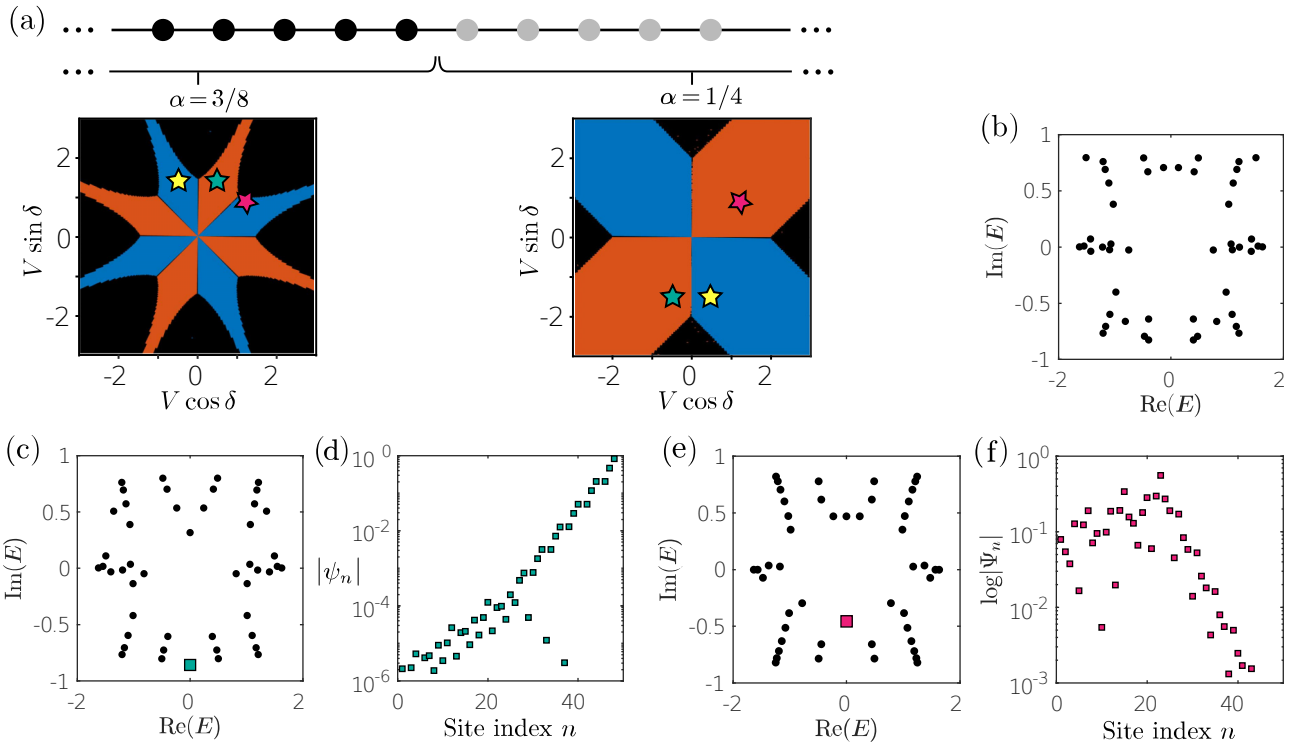

FIG. 10. (a) Schematic of a lattice with two domains of different modulation functions. The bottom panel shows the phase diagrams for the two domains, with different colored stars corresponding to the following panels. All other parameters are the same in Fig. 2 of the main text. (b) Complex spectrum for a trivial-trivial configuration [yellow stars in (a)]. (c) Complex spectrum for a nontrivial-nontrivial configuration [green stars in (a)]. (d) Spatial distribution of the zero mode indicated by the square marker in (c). (e) Complex spectrum for a nontrivial-trivial configuration [pink stars in (a)]. (f) Spatial distribution of the zero mode indicated by the square marker in (e).

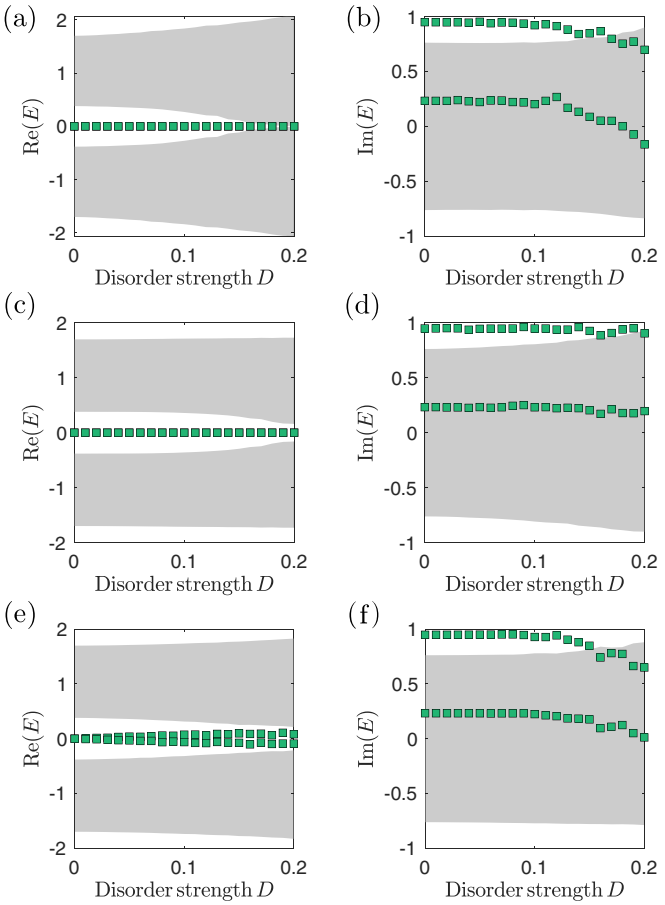

FIG. 11. Real and imaginary parts of the spectrum versus disorder strength D. The green squares are the eigenenergies closest to $\mathrm{Re}(E) = 0$, and the gray regions are the other eigenenergies. All eigenenergies are averaged over 100 disorder realizations for each D. Three types of disorder are studied: (a)–(b) purely real and reciprocal disorder in the nearest-neighbor hoppings; (c)–(d) purely imaginary on-site disorder; and (e)–(f) purely real on-site disorder. In each case, D times a normally distributed random number is added to each specified term in the Hamiltonian. All other model parameters are the same as in Fig. 1(b) of the main text.

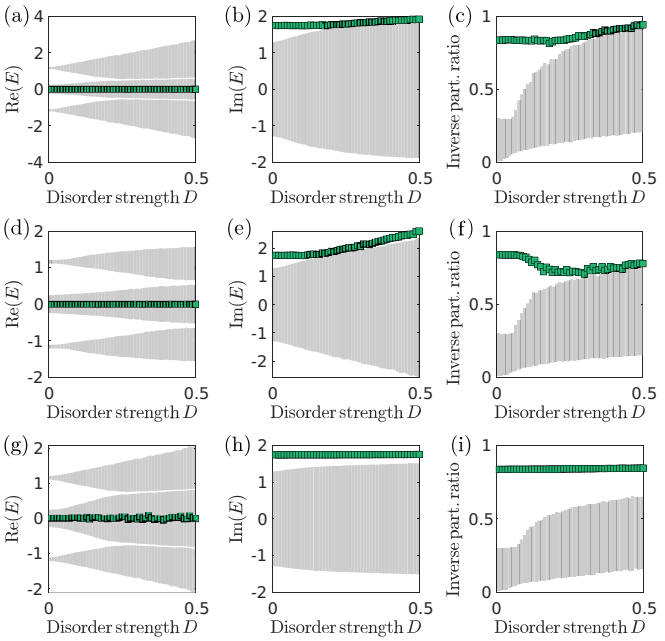

FIG. 12. Real [(a), (d), (g)] and imaginary [(b), (e), (h)] eigenenergies versus disorder strength D, in the absence of a real line gap. The edge modes (green squares) and the other modes in the complex band structure (gray areas) are plotted separately. The inverse participation ratio, a measure of localization [64], is also plotted in (c), (f), (i). The three rows, (a)–(c), (d)–(f), and (g)–(i), correspond to type (i), (ii), and (iii) disorder as described in the text. These results were obtained for $V\cos\delta = 0.48$, with all other parameters the same as in Figs. 3(b) and 3(c) of the main text.

square marker in Fig. 10(b), the spatial distribution is plotted in Fig. 10(c). The wave function is localized on an external boundary, rather than the domain wall. The other zero mode behaves similarly. In the final case, corresponding to the pink stars in Fig. 10(a), the left domain is topologically trivial and the right domain is topologically nontrivial (the opposite of what we considered in Fig. 2 of the main text). As shown in Fig. 10(e), there are zero modes in the complex spectrum. The spatial distribution of the mode indicated by a square marker is plotted in Fig. 10(f), revealing that the mode is exponentially localized to the domain wall.

APPENDIX E: ROBUSTNESS ANALYSIS AGAINST PERTURBATIONS

In this section, we study the robustness of the edge modes against three types of disorder:

(1) Disorder in the nearest-neighbor hoppings (real-valued, reciprocity-preserving disorder in the off-diagonal terms of the Hamiltonian).

(2) Disorder in the on-site gain/loss (the imaginary part of the diagonal terms of the Hamiltonian).

(3) Disorder in the on-site mass (the real part of the diagonal terms of the Hamiltonian).

Note that cases (i) and (ii) preserve the non-Hermitian particle-hole symmetry discussed in the paper, whereas case (iii) breaks this symmetry. In all cases, the disorder is implemented using random numbers drawn independently from a normal distribution, multiplied by a factor D that represents the disorder strength. The eigenvalues of the perturbed Hamiltonian are then numerically obtained. The procedure is repeated 100 times, and we plot the mean of E for the zero-energy modes (green squares), as well as the mean of the other eigenenergies in the complex band structure (gray area).

First, consider Figs. 11(a) and 11(b), which correspond to type-(i) disorder, and Figs. 11(c) and 11(d), which correspond to type-(ii) disorder. We see that increasing the disorder strength D broadens the real part of the bulk bands, narrowing the real band gap. However, the zero modes of the disorder-free lattice persist, and remain pinned to $\mathrm{Re}(E) = 0$, as the disorder strength is increased. This is due to these forms of disorder preserving the non-Hermitian particle-hole symmetry.

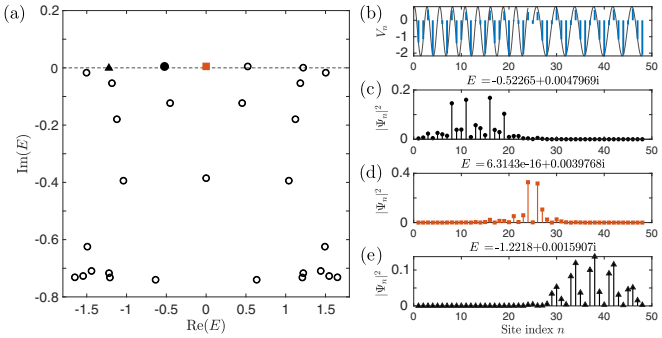

FIG. 13. (a) Distribution of complex eigenenergies in the multimode laser. The eigenenergies are calculated from the nonlinear Hamiltonian (obtained via the time domain simulations described in the paper), by time-averaging the intensity on each site to determine the gain saturation. The pump strength is $\Gamma = 0.8$. (b) Spatial distribution of the effective gain/loss V_n for the nonlinear (gain-saturated) lattice in (a) (blue bars). For comparison, we also plot the unsaturated gain/loss profile (black curves). (c)–(e) Distributions of the three eigenmodes marked by a triangle, circle, and square in (a); panel (d) corresponds to the domain wall state, which is also the threshold lasing mode. All model parameters are the same as in Figs. 4(d) and 4(e) of the main text.

For Figs. 11(e) and 11(f), which corresponds to type-(iii) disorder, the non-Hermitian particle-hole symmetry is not preserved, and the boundary state is not pinned to $\mathrm{Re}(E) = 0$. Note that a sufficiently large disorder strength D may reduce the effective gain of the edge mode, eventually making it lower than the effective gain of the bulk modes.

These results were obtained for $\alpha = 3/8$, with the disorder-free parameters chosen to be the same as in Fig. 1(b) of the main text. The results for other α (e.g., $\alpha = 1/4$ and $\alpha = 1/12$) are similar.

Using a similar approach, we investigated the stability of the edge modes in the gapless phase. Figure 12 shows the results for lattices with $V \cos\delta = 0.48$—a situation where the edge modes persist despite the absence of a real line gap, consistent with Fig. 3 of the main text. The same three types of disorder defined above, types (i)–(iii), are separately studied. The edge mode is identified by picking out the mode with the highest inverse participation ratio, a measure of mode localization [64]. In Figs. 12(a) and 12(d), we observe that the edge modes remain pinned at $\mathrm{Re}(E)$ with increasing disorder strength D, for the symmetry-preserving type (i) and (ii) disorder. For smaller values of D, the edge state still has the highest gain, but for larger D the edge state hybridizes with the bulk states, and becomes no longer distinguishable both in terms of $\mathrm{Im}(E)$ and the degree of localization. For type (iii) disorder, shown in Fig. 12(g), the gapless edge mode remains isolated from other bulk modes even for large D. This interesting phenomenon will be investigated in future work.

APPENDIX F: TRANSITION FROM SINGLE-MODE TO MULTIMODE LASING

In our study of the lasing properties of non-Hermitian AAH lattices, the transition to multimode lasing occurs because the pump strength becomes sufficiently large that the competing (nontopological) modes are also crossing their lasing thresholds (i.e., receiving net positive gain). This behavior is not specific to the present system or to topological lasers, but happens for many other laser systems that have multiple modes [39].

To show that this is indeed what happens in the present model, Fig. 13(a) plots the modal gains for the various modes at a typical pump strength ($\Gamma = 0.8$) in the multimode regime. These modal gains take account of gain saturation (a nonlinear effect), and are calculated from the eigenvalues of an effective nonlinear Hamiltonian obtained by inserting the mean intensity distribution (time-averaged over $t \in [2000, 5000]$) into Eq. (5) of the main text. As can be seen, aside from the zero mode (red square), several other modes have reached the threshold condition $\mathrm{Im}(E) = 0$. Three of the mode distributions are plotted in Figs. 13(c)–13(e); it can be seen that the additional lasing modes are not edgelike but arise from the bulk. Note that the case of Figs. 4(a) and 4(b) is similar to the situation here.

Figure 13(b) plots the nonlinear (i.e., inclusive of gain saturation) gain profile (blue bars). It is very similar to the unsaturated gain profile (black sinusoidal curves), aside from the sites near the domain wall. This is to be expected: the first lasing mode is the topological edge mode, so the gain is saturated near the domain wall and relatively unsaturated elsewhere.

[1] P. G. Harper, Single band motion of conduction electrons in a uniform magnetic field, Proc. Phys. Soc., Sect. A **68**, 874 (1955).

[2] S. Aubry and G. André, Analyticity breaking and Anderson localization in incommensurate lattices, Ann Isr. Phys. Soc. **3**, 133 (1980).

[3] D. J. Thouless, M. Kohmoto, M. P. Nightingale, and M. den Nijs, Quantized Hall Conductance in a Two-Dimensional Periodic Potential, Phys. Rev. Lett. **49**, 405 (1982).

[4] J. Faist, *Quasicrystals*, 1st ed. (Oxford University Press, Oxford, 1994).

[5] Y. E. Kraus and O. Zilberberg, Quasiperiodicity and topology transcend dimensions, Nat. Phys. **12**, 624 (2016).

[6] O. Zilberberg, Topology in quasicrystals, Opt. Mater. Express **11**, 1143 (2021).

[7] S. Ganeshan, K. Sun, and S. D. Sarma, Topological Zero-Energy Modes in Gapless Commensurate Aubry-André-Harper Models, Phys. Rev. Lett. **110**, 180403 (2013).

[8] S. Ryu and Y. Hatsugai, Topological Origin of Zero-Energy Edge States in Particle-Hole Symmetric Systems, Phys. Rev. Lett. **89**, 077002 (2002).

[9] A. Yu. Kitaev, Unpaired Majorana fermions in quantum wires, Phys. Usp. **44**, 131 (2001).

[10] S. Longhi, *PT*-symmetric optical superlattices, J. Phys. A: Math. Theor. **47**, 165302 (2014).

[11] C. Yuce, *PT*-symmetric Aubry-André model, Phys. Lett. A **378**, 2024 (2014).

[12] A. K. Harter, T. E. Lee, and Y. N. Joglekar, *PT*-breaking threshold in spatially asymmetric Aubry-André and Harper models: Hidden symmetry and topological states, Phys. Rev. A **93**, 062101 (2016).

[13] S. Longhi, Topological Phase Transition in Non-Hermitian Quasicrystals, Phys. Rev. Lett. **122**, 237601 (2019).

[14] H. Jiang, L. Lang, C. Yang, S. Zhu, and S. Chen, Interplay of non-Hermitian skin effects and Anderson localization in nonreciprocal quasiperiodic lattices, Phys. Rev. B **100**, 054301 (2019).

[15] Q. Zeng, Y. Yang, and R. Lü, Topological phases in one-dimensional nonreciprocal superlattices, Phys. Rev. B **101**, 125418 (2020).

[16] T. Liu, H. Guo, Y. Pu, and S. Longhi, Generalized Aubry-André self-duality and mobility edges in non-Hermitian quasiperiodic lattices, Phys. Rev. B **102**, 024205 (2020).

[17] Y. Liu, X. P. Jiang, J. Cao, and S. Chen, Non-Hermitian mobility edges in one-dimensional quasicrystals with parity-time symmetry, Phys. Rev. B **101**, 174205 (2020).

[18] S. Longhi, Phase transitions in a non-Hermitian Aubry-André-Harper model, Phys. Rev. B **103**, 054203 (2021).

[19] S. Weidemann, M. Kremer, S. Longhi, and A. Szameit, Topological triple phase transition in non-Hermitian Floquet quasicrystals, Nature (London) **601**, 354 (2022).

[20] Ş. K. Özdemir, S. Rotter, F. Nori, and L. Yang, Parity-time symmetry and exceptional points in photonics, Nat. Mater. **18**, 783 (2019).

[21] K. Kawabata, K. Shiozaki, M. Ueda, and M. Sato, Symmetry and Topology in Non-Hermitian Physics, Phys. Rev. X **9**, 041015 (2019).

[22] Y. Ashida, Z. Gong, and M. Ueda, Non-Hermitian Physics, Adv. Phys. **69**, 249 (2020).

[23] H. Schomerus, Topologically protected midgap states in complex photonic lattices, Opt. Lett. **38**, 1912 (2013).

[24] L. Lang, Y. Wang, H. Wang and Y. D. Chong, Effects of non-Hermiticity on Su-Schrieffer-Heeger defect states, Phys. Rev. B **98**, 094307 (2018).

[25] M. Pan, H. Zhao, P. Miao, S. Longhi and L. Feng, Photonic zero mode in a non-Hermitian photonic lattice, Nat. Commun. **9**, 1308 (2018).

[26] M. Parto, S. Wittek, H. Hodaei, G. Harari, M. A. Bandres, J. Ren, M. C. Rechtsman, M. Segev, D. N. Christodoulides and M. Khajavikhan, Edge-Mode Lasing in 1D Topological Active Arrays, Phys. Rev. Lett. **120**, 113901 (2018).

[27] H. Zhao, P. Miao, M. H. Teimourpour, S. Malzard, R. E. Ganainy, H. Schomerus and L. Feng, Topological hybrid silicon microlasers, Nat. Commun. **9**, 981 (2018).

[28] L. Ge, Symmetry-protected zero-mode laser with a tunable spatial profile, Phys. Rev. A **95**, 023812 (2017).

[29] B. Qi, L. Zhang, and L. Ge, Defect States Emerging from a Non-Hermitian Flatband of Photonic Zero Modes, Phys. Rev. Lett. **120**, 093901 (2018).

[30] T. E. Lee, Anomalous Edge State in a Non-Hermitian Lattice, Phys. Rev. Lett. **116**, 133903 (2016).

[31] D. Leykam, K. Y. Bliokh, C. Huang, Y. D. Chong, and F. Nori, Edge Modes, Degeneracies, and Topological Numbers in Non-Hermitian Systems, Phys. Rev. Lett. **118**, 040401 (2017).

[32] K. Takata and M. Notomi, Photonic Topological Insulating Phase Induced Solely by Gain and Loss, Phys. Rev. Lett. **121**, 213902 (2018).

[33] X. Luo and C. Zhang, Higher-Order Topological Corner States Induced by Gain and Loss, Phys. Rev. Lett. **123**, 073601 (2019).

[34] E. Lee, H. Lee, and B.-J. Yang, Many-body approach to non-Hermitian physics in fermionic systems, Phys. Rev. B **101**, 121109(R) (2020).

[35] C. Ortega-Taberner, L. Rødland, and M. Hermanns, Polarization and entanglement spectrum in non-Hermitian systems, Phys. Rev. B **105**, 075103 (2022).

[36] J. Hu, C. A. Perroni, G. D. Filippis, S. Zhuang, L. Marrucci, and F. Cardano, Electric polarization and its quantization in one-dimensional non-Hermitian chains, Phys. Rev. B **107**, L121101 (2023).

[37] P. St-Jean, V. Goblot, E. Galopin, A. Lemaître, T. Ozawa, L. Le Gratiet, I. Sagnes, J. Bloch, and A. Amo, Lasing in topological edge states of a one-dimensional lattice, Nat. Photonics **11**, 651 (2017).

[38] Y. Ota, R. Katsumi, K. Watanabe, S. Iwamoto and Y. Arakawa, Topological photonic crystal nanocavity laser, Commun. Phys. **1**, 86 (2018).

[39] G. Harari, M. A. Bandres, Y. Lumer, M. C. Rechtsman, Y. D. Chong, M. Khajavikhan, D. N. Christodoulides, and M. Segev, Topological insulator laser: Theory, Science **359**, eaar4003 (2018).

[40] M. A. Bandres, S. Wittek, G. Harari, M. Parto, J. Ren, M. Segev, D. N. Christodoulides, and M. Khajavikhan, Topological insulator laser: Experiments, Science **359**, eaar4005 (2018).

[41] Y. Zeng, U. Chattopadhyay, B. Zhu, B. Qiang, J. Li, Y. Jin, L. Li, A. G. Davies, E. H. Linfield, B. Zhang, Y. D. Chong, and Q. J. Wang, Electrically pumped topological laser with valley edge modes, Nature (London) **578**, 246 (2020).

[42] Z. Yang, Z. Shao, H. Chen, X. Mao, and R. Ma, Spin-Momentum-Locked Edge Mode for Topological Vortex Lasing, Phys. Rev. Lett. **125**, 013903 (2020).

[43] T. H. Harder, M. Sun, O. A. Egorov, I. Vakulchyk, J. Beierlein, P. Gagel, M. Emmerling, C. Schneider, U. Peschel, S. Klembt, and S. Hofling, Coherent topological polariton laser, ACS Photonics **8**, 1377 (2021).

[44] A. Dikopoltsev, T. H. Harder, E. Lustig, O. A. Egorov, J. Beierlein, A. Wolf, Y. Lumer, M. Emmerling, C. Schneider, S. Höfling, M. Segev, and S. Klembt, Topological insulator vertical-cavity laser array, Science **373**, 1514 (2021).

[45] J. H. Choi, W. E. Hayenga, Y. G. Liu, M. Parto, B. Bahari, D. N. Christodoulides, and M. Khajavikhan, Room temperature electrically pumped topological insulator lasers, Nat. Commun. **12**, 3434 (2021).

[46] B. Qi, H. Chen, L. Ge, P. Berini, and R. Ma, Parity-time symmetry synthetic lasers: Physics and devices, Adv. Opt. Mater. **7**, 1900694 (2019).

[47] E. J. Bergholtz, J. C. Budich, and F. K. Kunst, Exceptional topology of non-Hermitian systems, Rev. Mod. Phys. **93**, 015005 (2021).

[48] J. C. Garrison and E. M. Wright, Complex geometrical phases for dissipative systems, Phys. Lett. A **128**, 177 (1988).

[49] S. D. Liang and G. Y. Huang, Topological invariance and global Berry phase in non-Hermitian systems, Phys. Rev. A **87**, 012118 (2013).

[50] S. Lieu, Topological phases in the non-Hermitian Su-Schrieffer-Heeger model, Phys. Rev. B **97**, 045106 (2018).

[51] R. King-Smith and D. Vanderbilt, Theory of polarization of crystalline solids, Phys. Rev. B **47**, 1651 (1993).

[52] R. Resta, Quantum-Mechanical Position Operator in Extended Systems, Phys. Rev. Lett. **80**, 1800 (1998).

[53] W. A. Benalcazar, B. A. Bernevig, and T. L. Hughes, Electric multipole moments, topological multipole moment pumping, and chiral hinge states in crystalline insulators, Phys. Rev. B **96**, 245115 (2017).

[54] W. A. Benalcazar, B. A. Bernevig, and T. L. Hughes, Quantized electric multipole insulators, Science **357**, 61 (2017).

[55] M. Blanco de Paz, C. Devescovi, G. Giedke, J. J. Saenz, M. G. Vergniory, B. Bradlyn, D. Bercioux and A. Garciía Etxarri, Tutorial: Computing topological invariants in 2D photonic crystals, Adv. Quantum Technol. **3**, 1900117 (2020).

[56] P. Comaron, V. Shahnazaryan, W. Brzezicki, T. Hyart, and M. Matuszewski, Non-Hermitian topological end-mode lasing in polariton systems, Phys. Rev. Res. **2**, 022051(R) (2020).

[57] M. Wagner, F. Dangel, H. Cartarius, J. Main, and G. Wunner, Numerical calculation of the complex berry phase in non-Hermitian systems, Acta Polytech. **57**, 470 (2017).

[58] Y. E. Kraus, Y. Lahini, Z. Ringel, M. Verbin, and O. Zilberberg, Topological States and Adiabatic Pumping in Quasicrystals, Phys. Rev. Lett. **109**, 106402 (2012).

[59] M. Verbin, O. Zilberberg, Y. E. Kraus, Y. Lahini, and Y. Silberberg, Observation of Topological Phase Transitions in Photonic Quasicrystals, Phys. Rev. Lett. **110**, 076403 (2013).

[60] M. Verbin, O. Zilberberg, Y. Lahini, Y. E. Kraus, and Y. Silberberg, Topological pumping over a photonic Fibonacci quasicrystal, Phys. Rev. B **91**, 064201 (2015).

[61] W. A. Benalcazar and A. Cerjan, Bound states in the continuum of higher-order topological insulators, Phys. Rev. B **101**, 161116(R) (2020).

[62] A. Cerjan, M. Jürgensen, W. A. Benalcazar, S. Mukherjee, and M. C. Rechtsman, Observation of a Higher-Order Topological Bound State in the Continuum, Phys. Rev. Lett. **125**, 213901 (2020).

[63] Z. Yang, E. Lustig, G. Harari, Y. Plotnik, Y. Lumer, M. A. Bandres and M. Segev, Mode-Locked Topological Insulator Laser Utilizing Synthetic Dimensions, Phys. Rev. X **10**, 011059 (2020).

[64] D. J. Thouless, Electrons in disordered systems and the theory of localization, Phys. Rep. **13**, 93 (1974).